PAPER

The lifetime of interlayer breathing modes of few-layer 2H-MoSe$_2$ membranes†

Pedro Soubelet,[a] Andrés A. Reynoso,[a] Alejandro Fainstein, [ID][a] Karol Nogajewski, [ID][b,c] Marek Potemski,[b,c] Clément Faugeras*[c] and Axel E. Bruchhausen [ID] *[a]

A time-resolved observation of coherent interlayer longitudinal acoustic phonons in thin layers of 2H-MoSe$_2$ is reported. A femtosecond pump–probe technique is used to investigate the evolution of the energy loss of these vibrational modes in a wide selection of MoSe$_2$ flakes with different thicknesses ranging from bilayer up to the bulk limit. By directly analysing the temporal decay of the modes, we can clearly distinguish an abrupt crossover related to the acoustic mean free path of the phonons in a layered system, and the constraints imposed on the acoustic decay channels when reducing the dimensionality. For thicker samples, the main acoustic attenuation mechanism is attributed to the scattering of the acoustic modes with thermal phonons. For samples thinner than ~20 molecular layers, the predominant damping mechanism is ascribed to the effects of surface asperity. Losses intrinsic to the low dimensionality of single or few layer materials impose critical limitations for their use in optomechanical and optoelectronic devices.

1. Introduction

Two dimensional (2D) transition metal dichalcogenides (TMDCs)[1] combine many different unique properties such as high in-plane mobility,[2,3] relatively high heat conduction,[4,5] large Seebeck coefficients,[6] significant spin–orbit coupling,[1] together with remarkable mechanical properties.[7,8] Some members of this MX$_2$ family, with a 2H phase, where M is W or Mo and X is S, Se or Te, are semiconductors with relatively large indirect band gaps. In the form of monolayers, they become direct band gap semiconductors with strong excitonic effects and strong light–matter coupling at room temperature due to the reduced dimensionality.[9–11] They provide a strong luminescence, and they represent an interesting complement to gapless graphene mainly as photoactive materials in the NIR-Vis range. Applications seeking the conception of optoelectronic devices based on these TMDC nanomaterials,[12,13] ultrafast photodetection and light emission,[1,14,15] valleytronics and spintronics,[16] and field effect transistors (FETs)[1,3] based on

few layer van der Waals heterojunctions,[17,18] represent just a glimpse of the recent fruitful activity in the field.

Similar to graphene, TMDC monolayers constitute an uttermost 2D crystalline system composed of atoms linked by strong covalent bonds. In analogy to graphite, in a bulk TMDC crystal, these 2D-TMDC layers are stacked one on top of another and held together by "weak" van der Waals type interactions,[19] and exfoliation of ultra-pure bulk crystals is one technique that allows to isolate mono- and also few layers of these materials. MoSe$_2$ is the prototype of a 2D semiconductor with a bright exciton ground state[20] and a well defined emission spectrum.[21]

As in other materials, lattice vibrations (phonons) of these TMDCs play an essential role in determining their physical properties,[1,5,22] and mono- and few-layers of different TMDCs, especially semiconducting ones, have recently been the subject of intense investigations.[23–29] It is worth noting that layered crystals constitute a natural van der Waals structure,[19] and are hence an ideal system for probing interlayer vibrational modes and the cross-plane forces stand behind them.[30,31] One of the most elusive quantities in the studies of lattice vibrations has so far been the lifetime of phonons, in general, one of the least known properties of solid state systems. The reason for this should probably be ascribed to the experimental challenges associated with direct quantitative characterization of processes leading to phonon decay and coherence loss, as well as the complexity of modelling them.[32–37]

Since TMDCs exhibit strong correlations between electronic states and lattice vibrations,[29,38] which naturally affect a whole

[a]Centro Atómico Bariloche & Instituto Balseiro (CNEA) and CONICET,
8400 S.C. de Bariloche, R.N., Argentina. E-mail: axel.bruchhausen@cab.cnea.gov.ar
[b]Institute of Experimental Physics, Faculty of Physics, University of Warsaw,
Pasteura 5, 02-093 Warsaw, Poland
[c]Laboratoire National des Champs Magnétiques Intenses (CNRS, UJF, UPS, INSA),
BP 166, 38042 Grenoble Cedex 9, France. E-mail: clement.faugeras@lncmi.cnrs.fr
†Electronic supplementary information (ESI) available. See DOI: 10.1039/
C9NR02447F

range of fundamental properties of these materials, *e.g.* thermal transport, carrier mobility, light emission, among others,[1–11] having a good characterization of the phonon modes together with their damping (decay) rates is thus crucial to understand the possible decoherence channels that exist in these 2D-TMDC nanostructures, and are hence essential for the conception of electronic and optoelectronic devices.[12,39,40]

Only very few recent investigations have dealt with direct time-domain analysis of the actual dynamics of the electronic[41–45] and phononic[29,46–50] modes in TMDCs. In this paper, we focus on the temporal dynamics of a very particular acoustic phonon mode in 2H-MoSe$_2$, which tests the very nature of the interlayer forces: the acoustic interlayer breathing mode (B$_1$).[51,52] By tracing the phonon dynamics directly in the time-domain as a function of the number of MoSe$_2$ layers, covering a wide range of thicknesses, varying from 2, 3, ... individual layers up to a "bulk" situation, we are able to clearly evidence a profound change in the dominant phonon scattering mechanism affecting the lifetime of the breathing mode (τ_{B_1}).

2. Results

Samples and characterization

In order to isolate the crystal from possible interfering contact effects with the substrate,[23,53] the exfoliated 2H-MoSe$_2$ flakes were deposited on a specially designed substrate, which consisted of a (001) Si wafer with a 90 nm SiO$_2$ layer formed on-top of it, and where regular 6 μm diameter circular holes were patterned in the SiO$_2$. The flakes, after exfoliation from commercial bulk crystals provided by *HQ Graphene*, were randomly scattered on the substrate, and a careful selection enabled the identification of different flakes that were found free-standing on the holes, *i.e.* with no contact of the flakes' surfaces with the substrate. Fig. 1a displays an optical image with an example of several flakes scattered on the patterned substrate. We have identified the number of layers of the different flakes by their distinct optical contrast and with Raman scattering spectroscopy.[25,54] In Fig. 1a, the regions are labeled with the identified number of layers. The limiting border between different layer numbers, and the superposition with the underlying holes can be clearly observed.

It is important to mention that the low frequency geometric "drum-like" oscillations formed by the suspended region cannot be accessed with our experiment.[39,40] Our aim here is to analyse the *isolated* flakes, to be able to have a precise determination of the intrinsic temporal development of the internal "breathing" B$_1$ modes of bi- and few-layer membranes. When the samples are supported, the boundary conditions are changed considerably, modifying the acoustic dynamics and the time-domain signal.

Pump–probe spectroscopy

Fig. 1b shows a typical pump–probe set-up, such as the one used in this work. The 100 fs laser pulses are generated by using a Ti:Sapphire oscillator with an 80 MHz repetition rate
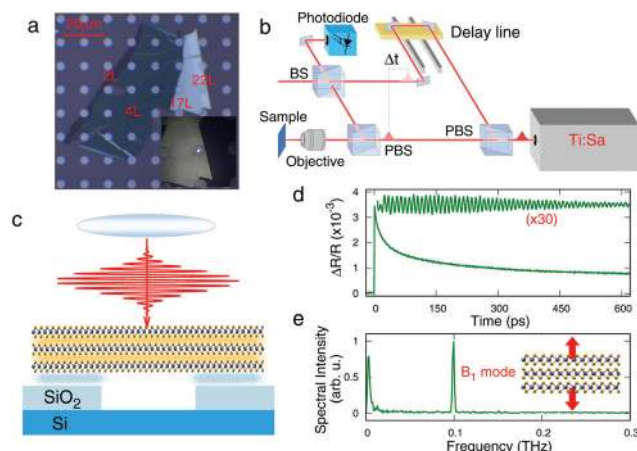

Fig. 1 Samples and experimental set up. (a) Optical image taken with a 50× objective of an exfoliated flake. The colour contrast outside the patterned holes enables the identification of sample thicknesses. The inset shows part of this image acquired with the 100× objective, where the laser spot is observed centred on top of the patterned hole of a sample with 22L. (b) Schematic diagram of the pump–probe setup. (c) Sketch of the incident laser pulse on a free-standing 3L MoSe$_2$ flake on top of a patterned hole. The shaded gaps in between MoSe$_2$ layers (yellow) and between MoSe$_2$ and SiO$_2$ (light-blue) indicate different van der Waals interactions. (d) Typically obtained transient reflectivity $\Delta R/R$ for 22L. The filtered signal displaying the coherent acoustic B$_1$ oscillations is shown on top (×30), and the corresponding numerical Fourier transform is depicted in (e). The inset in panel (e) exemplifies the dynamics of the B$_1$ mode for a 3L system.

and a central wavelength of about 805 nm. The laser was split in two, with the first more intense part (pump-beam) being focused directly onto the sample. The weaker part (probe-beam) was time-delayed with respect to the pump-beam using a mechanical delay-line, and focused spatially superimposed to the pump-beam onto the sample. All experiments were carried out at room temperature. Both beams, pump and probe, were focused co-linearly through the same 100× microscope objective (NA = 0.90), that could be simultaneously used to acquire a white light image (see the inset of Fig. 1a). The spot size was ∼1 μm and enabled the precise addressing of each individual free-standing MoSe$_2$ flake within one of the patterned holes, as is shown in the inset of Fig. 1a. Fig. 1c sketches this situation.

The temporal modulation of the reflection of the probe-beam $\Delta R(t)$, due to the changes in the optical constants by the impulsive excitation of vibrations induced by the pump-beam, was measured synchronously using a lock-in amplifier and a photo-diode. Fig. 1d shows a typical "as measured" transient obtained for a 22-layer (22L) flake, displaying a strong onset when both, pump and probe beams, coincide temporally ($t = 0$: zero delay-time), and relaxing multi-exponentially to its equilibrium. This behaviour mainly reflects the contribution of the electronic dynamics after the pump excitation to the temporal modulation of the optical constants. The signal on top (×30) shows the extracted high-frequency oscillation modes corresponding to the interlayer vibrational breathing B$_1$ mode,

which rings down with a characteristic damping time. Its numerical Fourier transform (nFT) is shown in Fig. 1e displaying a clear single peak with a frequency of about 0.1 THz. The inset sketches the B_1 optically active mode for an $MoSe_2$ system consisting of three layers (3Ls). Here, the two outer layers move in the opposite direction, indicated by the arrows.[23,30] The transient reflectivity pump–probe measurements have been performed on more than 20 free-standing $MoSe_2$ flakes, using typical mean powers of 400 μW and 100 μW for the pump and probe, respectively. In Fig. 2, examples of the extracted breathing mode oscillations, for samples with different number of layers, are displayed with red lines. The panels on the left side correspond to the coherently excited longitudinal acoustic oscillations in the time-domain, whereas the panels on the right side show the corresponding nFT of the oscillations. Note the strong change of the B_1 mode frequency and linewidth with the number of $MoSe_2$ layers. The fact that the damping time of the oscillations significantly shortens when reducing the number of layers is systematic and central for this work. This is also noticeable for the nFTs, where for the thicker samples (22L and 54L), the spectral width of the peaks is Fourier limited by the temporal window of observation. The frequency of the B_1-modes can be very well established (Fig. 3), and we can see that it can be as high as ~1 THz for the thinnest possible sample with two layers (2Ls), and shifts down when increasing the number of layers.

Linear chain model

B_1 longitudinal acoustic breathing phonon modes have been observed by Raman spectroscopy,[23,25,30,51] and are characterized by compressing–expanding the different layers against

Fig. 3 Mode frequency as a function of the inverse number of layers $1/N$. The blue squares correspond to the thinner samples in which the number of layers was experimentally identified. The full curve is the fitting with the linear chain model, and the red circles correspond to the thicker samples, where the values of N were determined by using the obtained value for f_o. The inset on the bottom right shows the details of these latter cases. The top-left inset corresponds to the calculated group velocity for the measured points, and the full curve corresponds to the calculated curve as a function of N (see the text for details regarding the model). The dashed lines indicate the result obtained for a continuum elastic model with the speed of sound v_{ac}.

each other, but leaving the internal structure within each individual layer intact (see the sketch in the inset of Fig. 1d), i.e. affecting only the weak interlayer forces. It has been proven for similar systems that a linear chain model with effective masses for each layer (per unit area, μ), and an effective interlayer elastic force (with an elastic constant per unit area, K) is well suited to describe these modes.[51,52] To solve the elastic equation of motion for the unsupported flakes, free-surface (stress-free) boundary conditions are proposed, resulting in the following well-known dispersion relation for the frequency of the modes as a function of the number of layers (N)[52]

$$f_{N,n} = f_o \sin\left(\frac{k_{N,n}d_o}{2}\right),\qquad(1)$$

where $d_o = 6.459$ Å (ref. 55) is the interlayer distance, $k_{N,n} = \frac{2\pi}{\lambda_{ac}}$, the associated acoustic wavelength is $\lambda_{ac} = \frac{2Nd_o}{n}$, f_o is related to the interlayer elastic constants and the effective mass as

$$f_o = \sqrt{\frac{K}{\pi^2\mu}},\qquad(2)$$

and $n = 1, 2, ...(N-1)$ corresponds to the mode index. For the purpose of the present investigation, we only consider the fundamental mode $n = 1$. For the thinner samples ($N = 2, 3, 4, 5$ and 8 layers), the number of layers can be well identified, and their obtained frequency is plotted in Fig. 3 with blue squares. These results are fitted with the above expression 1 obtaining a value for $f_o = (1.39 \pm 0.03)$ THz. The fitted curve is shown in
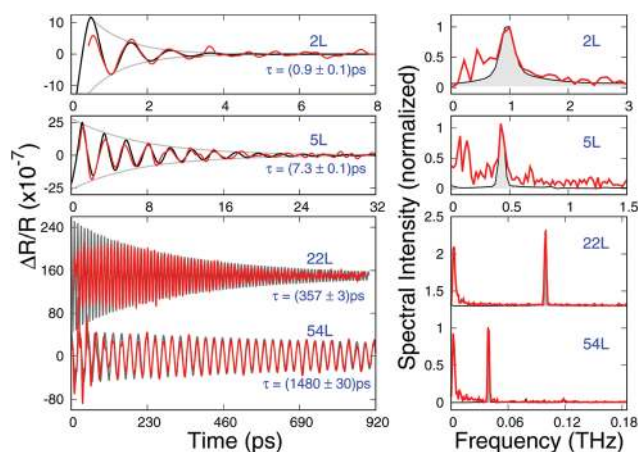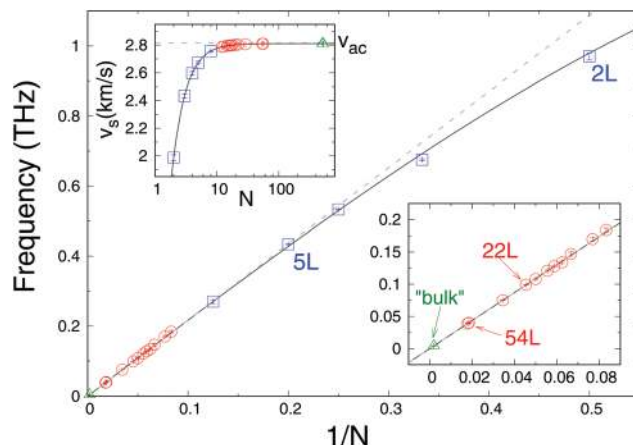
Fig. 2 Temporal and Fourier domains of the measured transients. Left: Experimental signals (red curves) in the time-domain showing the extracted oscillations corresponding to the B_1 mode for samples with different layer numbers (as indicated). Right: Numerical Fourier Transform of the corresponding transients. The black curves are the simulations that best fit the experiments simultaneously in the time and frequency domains. The obtained damping times τ are shown below each transient and the corresponding decaying exponential envelopes are indicated in grey.

Fig. 3 with the full curve. For thicker samples, the values of N can be determined by using the obtained value for f_o, the mode frequency obtained from the Fourier analysis (see *e.g.* Fig. 2, right panels), and deriving N from eqn (1). The results are plotted with red circles in Fig. 3. The inset on the right shows a close up for these cases. For the limiting case of a large N, the linear dependence is obtained. For thinner samples, a slight bending of the full line can be noticed, indicative of a sound speed reduction (see the top-left inset in Fig. 3). The overall agreement is very good. The dashed grey line corresponds to the case of a linear dispersion obtained using the continuum elastic model. The samples labelled as "bulk" (green triangle) actually corresponds to the largest N found and was estimated to be 519 ± 5 layers. An estimation for the in-plain effective mass for each layer, considering the atomic masses and the $MoSe_2$ the in-plane unit cell,[55] gives $\mu \simeq 4.41 \times 10^{-6}$ kg m^{-2}. From f_o obtained from the above fit, we can derive using eqn (2) an effective interlayer elastic force constant $K \simeq 8.42 \times 10^{19}$ N m^{-3}, consistent with other van der Waals materials.[30,51]

Given the above dispersion of eqn (1), it is possible to derive the longitudinal acoustic propagation velocity v_s in the stacking direction. This group velocity, defined as $\frac{d\omega}{dk}$ ($\omega = 2\pi f_N$), gives:

$$v_s(N) = \pi f_o d_o \cos\left(\frac{k_N d_o}{2}\right). \tag{3}$$

The upper left inset in Fig. 3 shows the calculated velocity for the corresponding points displayed in the main figure. The dashed curve in this inset corresponds to the interpolated calculated curve as a function of N. The asymptotic value for the "bulk" situation (large N), yields a "bulk" longitudinal acoustic sound velocity of $v_{ac} = \pi f_o d_o = 2820$ m s^{-1}. Notice that the low value of this velocity is compatible with the weak coupling between layers, and is similar to the values obtained for similar 2D TMDCs.[47,52]

Simulations

In order to gain a better understanding of the physical processes responsible for the generation and detection of these coherent longitudinal acoustic phonons and the resulting shape of the transient modulation of the probe reflectivity $\frac{\Delta R(t)}{R}$, we have modelled the complete acoustic impulsive generation and detection processes. The modelling considers the propagation and modification of the electromagnetic fields within the $MoSe_2$ membrane for the pump and probe pulses[56] and adapting the theory to include the elastic acoustic part accounting for the modes resulting from the linear chain model. The impulsive absorption of the pump pulse and the consequent phonon generation are described considering the displacive electro-optic mechanism,[56] whereas the coupling of the electromagnetic probe pulse and the phonons assumes a photo-elastic process,[56] *i.e.* longitudinal acoustic phonons modulate the dielectric susceptibility through the generated acoustic interlayer strain within the free-standing flake. In order to describe the temporal decay of the observed oscillations, we have introduced a dissipative term to the linear chain that adds the additional damping constant (τ^{-1}), where τ represents the acoustic damping time.

The results of the simulations, given the obtained values for N, the mode frequency f_N, and the bulk index of refraction for $MoSe_2$,[25] basically leaves two *a priori* uncorrelated parameters to adjust: first, the photo-elastic constant, which accounts only for a multiplicative constant;[56] and second, the damping time (τ). In Fig. 2, for the four samples, we exemplify how the simulations (black curves) fit the measured data. The agreement is quite remarkable for all cases in both domains, the temporal (left panels) as well as the spectral (right panels). The corresponding τ is indicated together with the used N. It is worth mentioning that both values are extremely critical for determining the central frequency and the correct *simultaneous* adjustment of the temporal traces and the spectral domain. Changing N in the ±1 layer, or modifying τ slightly, worsens the adjustment rapidly. The acoustic lifetimes are central to this work and of major interest for applications. In Fig. 4, we plot the obtained lifetimes τ for each of the measured samples, as a function of the corresponding frequency of the B_1-mode. The green triangles correspond to the lifetime obtained for the "bulk"-like samples, and have been derived
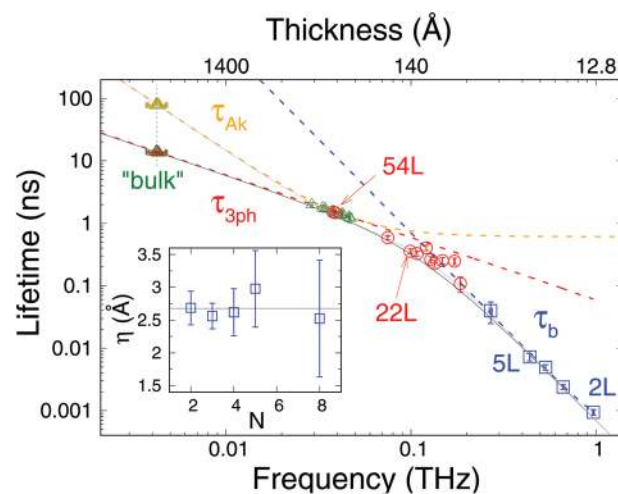

Fig. 4 Phonon lifetime τ as a function of the corresponding B_1-mode frequency. Those samples in which N was experimentally identified are plotted with blue squares and those in which it was determined by means of the fitted f_o are plotted with red circles. The simulation obtained using the three-phonon scattering model is plotted with the red dashed line (τ_{3ph}), and that when using the Akhiezer model is plotted with the orange dashed line (τ_{Ak}), and in blue the simulation accounting for the boundary scattering mechanism (τ_b). The total contribution to the mode lifetime can be estimated using the Matthiessen's rule and it is plotted with the grey line. The inset displays the asperity values obtained for each of the blue squares and the average is indicated by the horizontal line. The triangles correspond to the data obtained for the thicker samples. Those labelled as "bulk" indicate the corresponding extrapolated B_1 mode lifetime and the green triangles the measured higher harmonics (see the text for details).

from fitting the observed ΔR Brillouin comb ($2k_L$-modes), resulting from the fact that the optical penetration depth is smaller than the flake thickness.[54,57]

The general behaviour is that τ decreases for increasing phonon frequency, *i.e.* when the number of layers decreases. The evolution is rather linear for low and high frequencies (within the log–log scale), but a major and significant change in the slope above ~0.1 THz (*i.e.* below ~20 layers) can be clearly observed. Higher frequencies have a clear dependence that is proportional to f^{-3}, while the lower frequencies clearly depart from this slope, and rather follow $\propto f^{-1}$ evolution. This behaviour strongly suggests a fundamental change in the regime responsible for the energy loss of the observed longitudinal acoustic breathing B_1 modes, when lowering the number of layers.

3. Discussion

The intrinsic lifetime of propagating acoustic phonons in ultra-pure bulk matter is mainly determined by anharmonicity, *i.e.* the interaction of the coherently generated acoustic modes with the existing thermal phonon bath, through three-phonon-scattering processes.[34] Several methods have been proposed to calculate the phonon lifetime, but due to the complex nature of the different phonon–phonon interactions contributing to the decay channels, and despite the importance and technological interest, a complete general and rigorous modelling has been rather elusive. Several limiting cases have been treated, depending on the different regimes of relative temperature and acoustic frequencies.[34–37] At a given temperature, the damping rate τ^{-1} generally shows a polynomial-like dependence with the frequency ($\tau^{-1} \propto f^m$).[37]

We have analysed our results in the frame of two generally accepted approaches for describing the acoustic attenuation of the coherently generated modes, due to the interaction with the thermal phonons.[34–37] A first model, a Landau–Rumer-type of approach, based on the linearised Boltzmann equation in combination with a first order time-dependent perturbation theory to the anharmonic potential to account for the phonon–phonon scattering rates.[35–37] In particular, the three-phonon scattering rate is approximated using the single-mode relaxation time (SMRT) approximation, assuming a simple Debye model adapted for anisotropic materials,[58] and only including interactions of the observed B_1 modes with acoustic phonon branches of the membranes. The polarization of the observed modes is longitudinal (L). Consequently, we will *a priori* be considering three-phonon scattering (normal and umklapp) processes of the type

$$\omega_L + \omega_{s'} \rightarrow \omega_{s''} \quad \text{and} \quad \omega_L \rightarrow \omega_{s'} + \omega_{s''}. \quad (4)$$

Here, ω_L corresponds to the frequency of the observed B_1 mode, and $\omega_{s'}$ and $\omega_{s''}$ correspond to the frequencies of the other two modes involved in the process.

The inverse lifetime (τ^{-1}), *i.e.*, the relaxation rate, under this SMRT approximation is given by[37]

$$\tau_{3ph}^{-1} \propto \sum_{q's'q''s''} |A_{qq'q''}^{ss's''}|^2 \frac{qq'q''}{v_s v_{s'} v_{s''}} \delta_{q+q'+q'',G}$$
$$\left[\frac{\bar{n}_{s'}(\bar{n}_{s''}+1)}{\bar{n}_s+1} \delta(\omega_s+\omega_{s'}-\omega_{s''}) + \frac{1}{2} \frac{\bar{n}_{s'} \bar{n}_{s''}}{\bar{n}_s} \delta(\omega_s-\omega_{s'}-\omega_{s''}) \right]. \quad (5)$$

Here, $\bar{n}_s$ are the Bose–Einstein phonon distribution functions, and v_s and q are the speed of sound and wave vector of the phonons. A represents the three-phonon scattering strength of the anharmonic perturbation, which under certain assumptions, can be found to be proportional to an average Grüneisen parameter γ_{av}.[35–37] In Fig. 4, we plot with the red dashed line the result obtained within this model. Details of this calculation can be followed in the provided ESI.†[54] The remaining multiplying constant is fitted to best match the data for thicker samples (*i.e.* lower frequencies), and a $\gamma_{av}^{3ph} \simeq 1.8$ is derived, which is in rather good agreement with the calculated values found in the literature.[5] This approach yields a main dependence of $\tau_{3ph}^{-1} \propto f$, and well reproduces the experimental observation for $f < 0.1$ THz.[54]

The other model considered, follows the Akhiezer-type of approach,[34–37] where the coherently generated modes disturb the phonon thermal distribution. The presence of the thermal phonon population induces a viscosity that drives the system back into thermal equilibrium. The expression for the acoustic damping rate of the mode, that accounts for this mechanism, is of the form:[34–36,59]

$$\tau_{Ak}^{-1} = \frac{C_v T}{\rho v_{ac}^2} \frac{\omega^2 \tau_{th}}{1+\omega^2 \tau_{th}^2} (\gamma_{av}^{Ak})^2. \quad (6)$$

C_v and ρ are the volumetric heat capacity and mass density, respectively, and γ_{av}^{Ak} indicates the averaged Grüneisen parameter. τ_{th} represents the mean time between thermal phonon collisions and was estimated,[54] for the thermal transport kinetic formula, to be of the order of $\tau_{th} \sim 3$ ps.[34–36,59] $\gamma_{av}^{Ak} \simeq 0.74$ is chosen to best describe the data for $f < 0.1$ THz. The dashed-orange curve in Fig. 4 displays the corresponding result. For lower frequencies, this model yields $\tau_{Ak} \propto f^{-2}$, while for higher values, it becomes frequency independent.

Interestingly, the red dotted curve (τ_{3ph}) is basically tangent to the curve described by the Akhiezer-type of process at the frequency $f \sim 40$ GHz. As a consequence, extrapolating a value for the B_1-mode lifetime for the thicker "bulk"-like samples is ambiguous depending on which frequency dependence is considered (3ph or Ak). As mentioned above, the B_1-mode frequency is unambiguously determined by the frequency comb separation (indicated by the dotted vertical green line), and its derived "bulk" lifetime values are indicated by the triangles with the corresponding colour coding.

When lowering the dimensionality, *i.e.* restricting the acoustic propagation in one of the directions, surface effects become more important and change the dominant acoustic decay mechanism.[22] For thinner samples, a mechanism involving the sample *boundary* is expected to emerge. In order to describe the observed f^{-3} dependence, we model the decay

using an approach that accounts for the effects of surface *asperity* and the associated imperfect reflection of the vibrational acoustic modes. This simple model, proposed by Ziman back in the 60s[33,60] considers a mean free path (MFP) Λ of the travelling wave, determined by boundary scattering, which limits the phonon lifetime $\tau_b = \Lambda/v_s$. Within this approach $\Lambda = \frac{1+p}{1-p}\Lambda_o$, where p represents the mean acoustic surface specularity dependent on the phonon frequency, and Λ_o corresponds to the phonon MFP for perfectly rough (non-reflecting) surfaces. In our case, given the fact that the samples are thin, Λ_o is determined by the system characteristic dimensions, *i.e.* the flakes' nominal thickness $\frac{\lambda_{ac}}{2} = N d_o$.

Assuming small variations in the flake thickness, and the associated surface *asperity* to be η, defined as the root-mean-square deviation of these variations, the frequency-dependent specularity takes the form $p(f) = \exp[-16\pi^2\eta^2/\lambda_{ac}^2]$.[60] Consequently, the contribution to the lifetime due to the boundary scattering takes the form:[60]

$$\tau_b = \frac{\lambda_{ac}}{2v_s}\coth\left(\frac{8\pi^2\eta^2}{\lambda_{ac}^2}\right). \tag{7}$$

This expression, within a continuous elastic approximation, turns out to be proportional to f^{-3} (λ_{ac}^3).[54] The inset in Fig. 4 displays the individual calculated values of asperity as a function of N obtained by using the experimental values of τ for the thinnest samples (blue squares), the acoustic speed of sound from eqn (3) and (7). The average asperity $\bar{\eta} \sim 2.6$ Å is indicated by the horizontal grey line. The blue dashed curve in Fig. 4 shows the result using the above expression (7), and the derived mean value for $\bar{\eta}$. Notice that this value for asperity represents 20% of the bi-layer thickness. With our pump probe experiment, we are probing the material properties on a μm spatial scale, and optical images show, through the optical contrast analysis, a homogeneity at much larger scales. The value deduced for $\bar{\eta}$ is thus reasonable, and describes most probably defects at the surfaces with a reduced spatial extent. Such defects have been observed for flakes exposed to ambient conditions with local probe techniques and can be attributed to changes in the inter atomic bonding of surface atoms and impurities, dislocations, surface wrinkling, strain, and vacancies (most probably of Se atoms).[61,62]

For completeness, the lifetime accounting for the full acoustic frequency range can be obtained by combining both contributions, using the Matthiesen's rule $\tau^{-1} = \tau_{3ph}^{-1} + \tau_b^{-1}$ or $\tau^{-1} = \tau_{Ak}^{-1} + \tau_b^{-1}$.[37] The results for the combined lifetimes are shown in Fig. 4 with the full grey lines. As can be observed, τ very well describes the evolution of the acoustic mode lifetime in the whole frequency range.

4. Conclusions

In conclusion, we have analysed using ultrafast optical spectroscopy the dynamics of longitudinal acoustic vibrational modes in MoSe$_2$ exfoliated flakes, for varying thicknesses spanning from bulk like samples to few-layer systems, down to a MoSe$_2$-bilayer. The measured frequencies of the modes vary from 4.2 GHz up to 1 THz. By modelling the complete optical process of acoustic coherent impulsive generation and detection, we are able to precisely obtain the acoustic lifetime of the observed modes as a function of the flake layer number, *i.e.* the mode frequency. A clear and strong change in the lifetime dependence with frequency is evidenced, which is associated with a takeover between the acoustic phonon dephasing mechanism. Phenomenological models help to understand the dominating phonon scattering processes involved in each of the frequency regions, where for thicker samples, the anharmonic decay *via* phonon–phonon scattering dominates, while for thinner samples, where the acoustic mean free path becomes of the order of the flake thickness, the dominant decay process is driven by surface boundary scattering. A combination of both models gives a quantitative description for the full span of analysed membranes.

Given the intimate relation of the thermal conductivity with the phonon relaxation times,[34,60] these results are important to understand several properties such as thermal conductivity in the stacking direction in these transition metal dichalcogenides, which are of interest for several applications. In addition, free-standing single or few layered 2D-materials, in particular 2D-TMDCs, constitute unique efficient non-linear optomechanical systems,[13,39] and are used as high quality-factor resonators within the megahertz frequency range,[39] and as tunable ultra-low mass photonic mirrors with strong and fast optical responses.[12] Mechanical modes with frequencies approaching terahertz, as those observed in this work, are optically achieved and modulate the interlayer distances. The strong excitonic resonant effects and the large optomechanical coupling in these materials, associated with the ultra-fast strain modulation generated with relatively low-light excitation densities,[38] together with the possibility of combining other 2D materials with different and complementary physical properties at the nanoscale *via* van der Waals heterostructuring,[17] open interesting paths to establish promising opportunities for the design of devices for cavity nano-optomechanical applications,[13,38,63,64] eventually exploring cavity-less optomechanics,[65] working in the sub-terahertz regime, where the lifetime of the involved vibrations can be decisive in their performance.

Conflicts of interest

There are no conflicts to declare.

Acknowledgements

References

1 Q. H. Wang, K. Kalantar-Zadeh, A. Kis, J. N. Coleman and M. S. Strano, *Nat. Nanotechnol.*, 2012, **7**, 699–712.

2 A. Ayari, E. Cobas, O. Ogundadegbe and M. Fuhrer, *J. Appl. Phys.*, 2007, **101**, 014507.

3 H. Nam, B.-R. Oh, P. Chen, M. Chen, S. Wi, W. Wan, K. Kurabayashi and X. Liang, *Sci. Rep.*, 2015, **5**, 10546.

4 C. Faugeras, B. Faugeras, M. Orlita, M. Potemski, R. R. Nair and A. K. Geim, *ACS Nano*, 2010, **4**, 1889–1892.

5 B. Peng, H. Zhang, H. Shao, Y. Xu, X. Zhang and H. Zhu, *RSC Adv.*, 2016, **6**, 5767–5773.

6 M. Buscema, M. Barkelid, V. Zwiller, H. S. J. van der Zant, G. A. Steele and A. Castellanos-Gomez, *Nano Lett.*, 2013, **13**, 358–363.

7 A. Castellanos-Gomez, M. Poot, G. A. Steele, H. S. J. van der Zant, N. Agraït and G. Rubio-Bollinger, *Adv. Mater.*, 2012, **24**, 772–775.

8 R. C. Cooper, C. Lee, C. A. Marianetti, X. Wei, J. Hone and J. W. Kysar, *Phys. Rev. B: Condens. Matter Mater. Phys.*, 2013, **87**, 035423.

9 G. Wang, A. Chernikov, M. M. Glazov, T. F. Heinz, X. Marie, T. Amand and B. Urbaszek, *Rev. Mod. Phys.*, 2018, **90**, 021001.

10 A. Splendiani, L. Sun, Y. Zhang, T. Li, J. Kim, C.-Y. Chim, G. Galli and F. Wang, *Nano Lett.*, 2010, **10**, 1271–1275.

11 K. F. Mak, C. Lee, J. Hone, J. Shan and T. F. Heinz, *Phys. Rev. Lett.*, 2010, **105**, 136805.

12 P. Back, S. Zeytinoglu, A. Ijaz, M. Kroner and A. Imamoğlu, *Phys. Rev. Lett.*, 2018, **120**, 037401.

13 N. Morell, S. Tepsic, A. Reserbat-Plantey, A. Cepellotti, M. Manca, I. Epstein, A. Isacsson, X. Marie, F. Mauri and A. Bachtold, *Nano Lett.*, 2019, **91**(5), 3143–3150.

14 H. Huang, J. Wang, W. Hu, L. Liao, P. Wang, X. Wang, F. Gong, Y. Chen, G. Wu, W. Luo, H. Shen, T. Lin, J. Sun, X. Meng, X. Chen and J. Chu, *Nanotechnology*, 2016, **27**, 445201.

15 Y.-Q. Bie, G. Grosso, M. Heuck, M. M. Furchi, J. Z. Yuan Cao, D. Bunandar, E. Navarro-Moratalla, L. Zhou, D. K. Efetov, T. Taniguchi, K. Watanabe, J. Kong, D. Englund and P. Jarillo-Herrero, *Nanotechnology*, 2017, **12**, 1124–1129.

16 J. R. Schaibley, H. Yu, G. Clark, P. Rivera, J. S. Ross, K. L. Seyler, W. Yao and X. Xu, *Nat. Rev. Mater.*, 2016, **1**, 16055.

17 M. Huang, S. Li, Z. Zhang, X. Xiong, X. Li and Y. Wu, *Nat. Nanotechnol.*, 2017, **12**, 1148–1154.

18 S. Larentis, B. Fallahazad and E. Tutuc, *Appl. Phys. Lett.*, 2012, **101**, 223104.

19 A. K. Geim and I. V. Grigorieva, *Nature*, 2013, **499**, 419.

20 M. R. Molas, C. Faugeras, A. O. Slobodeniuk, K. Nogajewski, M. Bartos, D. M. Basko and M. Potemski, *2D Mater.*, 2017, **4**, 021003.

21 A. Arora, K. Nogajewski, M. Molas, M. Koperski and M. Potemski, *Nanoscale*, 2015, **7**, 20769–20775.

22 S. Ghosh, W. Bao, D. L. Nika, S. Subrina, E. P. Pokatilov, C. N. Lau and A. A. Balandin, *Nat. Mater.*, 2010, **9**, 555–558.

23 X. Lu, X. Luo, J. Zhang, S. Y. Quek and Q. Xiong, *Nano Res.*, 2016, **9**, 3559–3597.

24 A. Molina-Sánchez, K. Hummer and L. Wirtz, *Surf. Sci. Rep.*, 2015, **70**, 554–586.

25 P. Soubelet, A. E. Bruchhausen, A. Fainstein, K. Nogajewski and C. Faugeras, *Phys. Rev. B: Condens. Matter Mater. Phys.*, 2016, **93**, 155407.

26 S. Tongay, J. Zhou, C. Ataca, K. Lo, T. S. Matthews, J. Li, J. C. Grossman and J. Wu, *Nano Lett.*, 2012, **12**, 5576–5580.

27 P. Tonndorf, R. Schmidt, P. Böttger, X. Zhang, J. Börner, A. Liebig, M. Albrecht, C. Kloc, O. Gordan, D. R. T. Zahn, S. M. de Vasconcellos and R. Bratschitsch, *Opt. Express*, 2013, **21**, 4908–4916.

28 N. Kumar, Q. Cui, F. Ceballos, D. He, Y. Wang and H. Zhao, *Nanoscale*, 2014, **6**, 4915–4919.

29 M.-F. Lin, V. Kochat, A. Krishnamoorthy, L. Bassman, C. Weninger, Q. Zheng, X. Zhang, A. Apte, C. S. Tiwary, X. Shen, R. Li, R. Kalia, P. Ajayan, A. Nakano, P. Vashishta, F. Shimojo, X. Wang, D. M. Fritz and U. Bergmann, *Nat. Commun.*, 2017, **8**, 1745.

30 Y. Zhao, X. Luo, H. Li, J. Zhang, P. T. Araujo, C. K. Gan, J. Wu, H. Zhang, S. Y. Quek, M. S. Dresselhaus and Q. Xiong, *Nano Lett.*, 2013, **13**, 1007–1015.

31 X. Zhang, W. P. Han, J. B. Wu, S. Milana, Y. Lu, Q. Q. Li, A. C. Ferrari and P. H. Tan, *Phys. Rev. B: Condens. Matter Mater. Phys.*, 2013, **87**, 115413.

32 A. Bruchhausen, R. Gebs, F. Hudert, D. Issenmann, G. Klatt, A. Bartels, O. Schecker, R. Waitz, A. Erbe, E. Scheer, J.-R. Huntzinger, A. Mlayah and T. Dekorsy, *Phys. Rev. Lett.*, 2011, **106**, 077401.

33 J. Cuffe, O. Ristow, E. Chávez, A. Shchepetov, P.-O. Chapuis, F. Alzina, M. Hettich, M. Prunnila, J. Ahopelto, T. Dekorsy and C. M. Sotomayor Torres, *Phys. Rev. Lett.*, 2013, **110**, 095503.

34 H. J. Maris, *Physical Acoustics: Principles and Methods*, Academic Press, New York and London, 1st edn, 1971, vol. 8, ch. 6, pp. 279–336.

35 P. G. Klemens, *Physical Acoustics: Principles and Methods*, Academic Press, New York and London, 1st edn, 1965, vol. 3, part B, ch. 5, pp. 201–234.

36 R. Truell, C. Elbaum and B. B. Chick, *Ultrasonic Methods in Solid State Physics*, Academic Press, 1st edn, 1969, pp. 307–328 and Appendix I and J.

37 G. P. Srivastava, *The Physics of Phonons*, Adam Hilger, NY, 1st edn, 1990.

38 E. M. Mannebach, C. Nyby, F. Ernst, Y. Zhou, J. Tolsma, Y. Li, M.-J. Sher, I.-C. Tung, H. Zhou, Q. Zhang, K. L. Seyler,

G. Clark, Y. Lin, D. Zhu, J. M. Glownia, M. E. Kozina, S. Song, S. Nelson, A. Mehta, Y. Yu, A. Pant, O. B. Aslan, A. Raja, Y. Guo, A. DiChiara, W. Mao, L. Cao, S. Tongay, J. Sun, D. J. Singh, T. F. Heinz, X. Xu, A. H. MacDonald, E. Reed, H. Wen and A. M. Lindenberg, *Nano Lett.*, 2017, **17**, 7761–7766.

39 N. Morell, A. Reserbat-Plantey, I. Tsioutsios, K. G. Schädler, F. Dubin, F. H. L. Koppens and A. Bachtold, *Nano Lett.*, 2016, **16**, 5102–5108.

40 J. Güttinger, A. Noury, P. Weber, A. M. Eriksson, C. Lagoin, J. Moser, C. Eichler, A. Wallraff, A. Isacsson and A. Bachtold, *Nat. Nanotechnol.*, 2017, **12**, 631.

41 H. Shi, R. Yan, S. Bertolazzi, J. Brivio, B. Gao, A. Kis, D. Jena, H. G. Xing and L. Huang, *ACS Nano*, 2013, **7**, 1072–1080.

42 Q. Wang, S. Ge, X. Li, J. Qiu, Y. Ji, J. Feng and D. Sun, *ACS Nano*, 2013, **7**, 11087–11093.

43 E. M. Mannebach, K.-A. N. Duerloo, L. A. Pellouchoud, M.-J. Sher, S. Nah, Y.-H. Kuo, Y. Yu, A. F. Marshall, L. Cao, E. J. Reed and A. M. Lindenberg, *ACS Nano*, 2014, **8**, 10734–10742.

44 K. J. Czech, B. J. Thompson, S. Kain, Q. Ding, M. J. Shearer, R. J. Hamers, S. Jin and J. C. Wright, *ACS Nano*, 2015, **9**, 12146–12157.

45 F. Ceballos and H. Zhao, *Adv. Funct. Mater.*, 2017, **27**, 1616–3028.

46 D. Boschetto, L. Malard, C. H. Lui, K. F. Mak, Z. Li, H. Yan and T. F. Heinz, *Nano Lett.*, 2013, **13**, 4620–4623.

47 S. Ge, X. Liu, X. Qiao, Q. Wang, Z. Xu, J. Qiu, P.-H. Tan, J. Zhao and D. Sun, *Sci. Rep.*, 2014, **4**, 5722.

48 T. Y. Jeong, B. M. Jin, S. H. Rhim, L. Debbichi, J. Park, Y. D. Jang, H. R. Lee, D.-H. Chae, D. Lee, Y.-H. Kim, S. Jung and K. J. Yee, *ACS Nano*, 2016, **10**, 5560–5566.

49 B. He, C. Zhang, W. Zhu, Y. Li, S. Liu, X. Zhu, X. Wu, X. Wang, H.-h. Wen and M. Xiao, *Sci. Rep.*, 2016, **6**, 30487.

50 T. Kim, D. Ding, J.-H. Yim, Y.-D. Jho and A. J. Minnich, *APL Mater.*, 2017, **5**, 086105.

51 G. Froehlicher, E. Lorchat, F. Fernique, C. Joshi, A. Molina-Sánchez, L. Wirtz and S. Berciaud, *Nano Lett.*, 2015, **15**, 6481–6489.

52 L. Liang, J. Zhang, B. G. Sumpter, Q.-H. Tan, P.-H. Tan and V. Meunier, *ACS Nano*, 2017, **11**, 11777–11802.

53 M. Buscema, G. A. Steele, H. S. J. van der Zant and A. Castellanos-Gomez, *Nano Res.*, 2014, **7**, 561–571.

54 See the ESI† for further details.

55 A. Roy, H. C. P. Movva, B. Satpati, K. Kim, R. Dey, A. Rai, T. Pramanik, S. Guchhait, E. Tutuc and S. K. Banerjee, *ACS Appl. Mater. Interfaces*, 2016, **8**, 7396–7402.

56 M. F. Pascual-Winter, A. Fainstein, B. Jusserand, B. Perrin and A. Lemaître, *Phys. Rev. B: Condens. Matter Mater. Phys.*, 2012, **85**, 235443.

57 M. Grossmann, M. Klingele, P. Scheel, O. Ristow, M. Hettich, C. He, R. Waitz, M. Schubert, A. Bruchhausen, V. Gusev, E. Scheer and T. Dekorsy, *Phys. Rev. B: Condens. Matter Mater. Phys.*, 2013, **88**, 205202.

58 Z. Chen, Z. Wei, Y. Chen and C. Dames, *Phys. Rev. B: Condens. Matter Mater. Phys.*, 2013, **87**, 125426.

59 B. C. Daly, K. Kang, Y. Wang and D. G. Cahill, *Phys. Rev. B: Condens. Matter Mater. Phys.*, 2009, **80**, 174112.

60 J. M. Ziman, *Electrons and Phonons, The Theory of Transport Phenomena in Solids*, Oxford University Press, Oxford, 1st edn, 1960, pp. 450–482.

61 S. Dubey, S. Lisi, G. Nayak, F. Herziger, V.-D. Nguyen, T. Le Quang, V. Cherkez, C. González, Y. J. Dappe, K. Watanabe, T. Taniguchi, L. Magaud, P. Mallet, J.-Y. Veuillen, R. Arenal, L. Marty, J. Renard, N. Bendiab, J. Coraux and V. Bouchiat, *ACS Nano*, 2017, **11**, 11206–11216.

62 A. Shafqat, T. Iqbal and A. Majid, *AIP Adv.*, 2017, **7**, 105306.

63 X. Gao, Z.-q. Yin and T. Li, 2017, arXiv:1712.09245v1 [quant-ph].

64 P. Weber, J. Güttinger, A. Noury, J. Vergara-Cruz and A. Bachtold, *Nat. Commun.*, 2016, **7**, 12496.

65 H. Okamoto, T. Watanabe, R. Ohta, K. Onomitsu, H. Gotoh, T. Sogawa and H. Yamaguchi, *Nat. Commun.*, 2015, **6**, 8478.